Heteroatom- and bonded Z-scheme channels-Modulated Ultrafast Carrier Dynamics and Exciton Dissociation in Covalent Triazine Frameworks for Efficient Photocatalytic Hydrogen Evolution

Rongchen Shen[a+], Neng Li[b+], Chaochao Qin[c+], Xiuzhi Li[c], Peng Zhang[d], Xin Li[a], Junwang Tang[e*]*

[a] Dr. R. Shen, Prof. X. Li
Institute of Biomass Engineering, Key Laboratory of Energy Plants Resource and Utilization, Ministry of Agriculture and Rural Affairs, South China Agricultural University, Guangzhou 510642, China
E-mail: Xinli@scau.edu.cn

[b] Prof. N. Li
State Key Laboratory of Silicate Materials for Architectures, Wuhan University of Technology, Hubei, 430070, China E-mail: lineng@whut.edu.cn

[c] Dr. X. Li, Prof. C. Qing
Henan Key Laboratory of Infrared Materials and Spectrum Measures and Applications, School of Physics, Henan Normal University, Xinxiang 453007, Henan, China.

[d] Prof. P. Zhang
State Centre for International Cooperation on Designer Low-Carbon & Environmental Materials (CDLCEM), School of Materials Science and Engineering, Zhengzhou University, Henan, Zhengzhou, 450001, P. R. China

[e] Prof. J. Tang
Department of Chemical Engineering, University College London, London WC1E 7JE, UK. E-mail: junwang.tang@ucl.ac.uk

[+] These authors contributed equally to this work

KEYWORDS *Z-scheme heterojunction • Exciton Dissociation • Photocatalytic hydrogen evolution • Charge separation • Phosphorus-incorporated Covalent Triazine Frameworks*

Abstract

Covalent triazine frameworks **(**CTF) offer a tunable platform for photocatalytic H_2 generation due to their diverse structures, low costs, and precisely tunable electronic structures. However, high exciton binding energy and short lifetimes of photogenerated carriers restrict its application in photocatalytic hydrogen evolution. Herein, a novel phosphorus-incorporated CTF is introduced to construct a precisely bonded PCTF/WO_3 (PCTFW) heterostructure with a precise interface electron transfer channel. The phosphorus incorporation was found to dominantly reduce the exciton binding energy and promote the dissociation of singlet and triplet excitons into free charge carriers due to the regulation of electronic structures. High-quality interfacial W-N bonds improve the interfacial transfer of photogenerated electrons, thus prolonging the lifetime of photogenerated electrons. Femtosecond transient absorption spectroscopy characterizations and DFT calculations further confirm both phosphorus incorporation and Z-scheme heterojunctions could synergistically boost the in-built electric field and accelerate the migration and separation of photogenerated electrons. The optimized photocatalytic H_2-evolution rate of resultant PCTF-WO_3 (PCTFW) was 134.84 μmol h^{-1} (67.42 mmol $h^{-1}g^{-1}$), with an apparent quantum efficiency of 37.63% at 420 nm, surpassing many reported CTF-based photocatalysts so far. This work highlights the significance of atom-level precise exciton dissociation, and transfer and separation of interfacial and surface electrons in improving photocatalysis.

1. Introduction

Covalent triazine frameworks (CTFs) as crystallized conjugated porous polymers have received a lot of attention in recent years due to their diverse structures, abundant compositional elements (C, H, O, N, and S), and precisely tunable electronic structures[1]. Therefore, low-cost CTFs have witnessed the rapid development of photocatalytic hydrogen evolution reactions (HER). Nonetheless, the large exciton binding energy, short exciton

diffusion lengths[2], and fast charge recombination could cause superfast exciton recombination in the semiconductor bulk, thereby hindering the photocatalytic HER rates of these CTFs, thus making them confined within 10 mmol $h^{-1}g^{-1}$ [3]. Therefore, the development of high-activity and durable CTF-based H_2-evolution photocatalysts (HEPs) with better exciton dissociation and light absorption above 500 nm has proved to be more challenging.

To overcome this limitation, substantial efforts should focus on boosting exciton dissociation to develop more efficient organic semiconductor photocatalysts. Notably, several effective strategies, such as enhancing the crystalline and hydrophilicity, creating an intramolecular donor−acceptor (D−A) interaction [4], incorporating order−disorder interfaces[5] and substitution of highly electronegative elements(i.e., fluorine)[6], have been proposed to improve the exciton dissociation in organic semiconductors. Not long ago, Xie et al. demonstrated that the coexisting, competitive exciton generation affects the production of free charge carriers in inorganic BiOBr, which was necessary for photocatalytic hydrogen evolution.[7] Especially, excitonic effects in organic semiconductors are much stronger than inorganic ones. Therefore, accelerating the dissociation of excitons will fundamentally boost charge-carrier-involved photocatalysis.[8] However, the traditional study dominantly focuses on separating photogenerated charge pairs, which are somehow incomprehensive due to exciton effects that have long been ignored. Typically, constructing donor-acceptor (D–A) type organic semiconductors with high crystalline could boost the exciton dissociation ability[5, 9]. However, precisely tailoring the photoactive building/molecular units and band structure is more demanding and challenging in this system for achieving better photocatalysis. Inspired by the strategy of heteroatom incorporation in the g-C_3N_4-based semiconductor[10], we envision exploiting their potential roles of heteroatom incorporation in improving exciton dissociation in CTFs. In the photocatalytic area, heteroatom incorporation has been widely used as one of the most effective methods to optimize the absorption range, charge separation and migration, or in-built electric field[10c]. In contrast, the potential impacts

of heteroatom incorporation on excitonic effects are still unknown. To this end, no study about incorporating CTF with heteroatoms has been achieved. Moreover, a poor mechanistic understanding of the incorporation-induced change in surface properties and electronic structures on CTF will hinder the rational design and fabrication of doped CTF photocatalysts. In this aspect, the incorporation of CTF with P heteroatoms is thus highly promising and appealing. Therefore, we reasonably propose that P incorporation in CTF (PCTF) can be more readily fabricated for improving photocatalytic hydrogen evolution, which also contributes deeper understanding and the better unraveling of the structure-activity relationship in P-incorporated CTF and its heterojunction and the maximum utilization of charge carriers from efficient exciton dissociation.

Herein, we demonstrate that the doped P heteroatoms can efficiently boost exciton dissociation for the first time, giving rise to improved charge-carrier production. Then, we combine PCTF with WO_3 (PCTFW) to format precisely connected Z-scheme heterojunctions to enhance the charge separation and stability of PCTF. Through femtosecond transient absorption spectroscopy, fluorescence spectra, phosphorescence spectra and Density functional theory (DFT) computational study, the introduced P atoms could be found to simultaneously boost the built-in electric fields of CTF and induce exciton to dissociate into charge carriers. Furthermore, benefiting from the charge-carrier generating and separating, PCTFW displayed excellent photocatalytic hydrogen evolution performance. The unique design strategies proposed in this work provide a new approach to exploring efficient hydrogen-production photocatalysts for practical application.

2. Result and discussion

2. 1 Characterizations of Materials

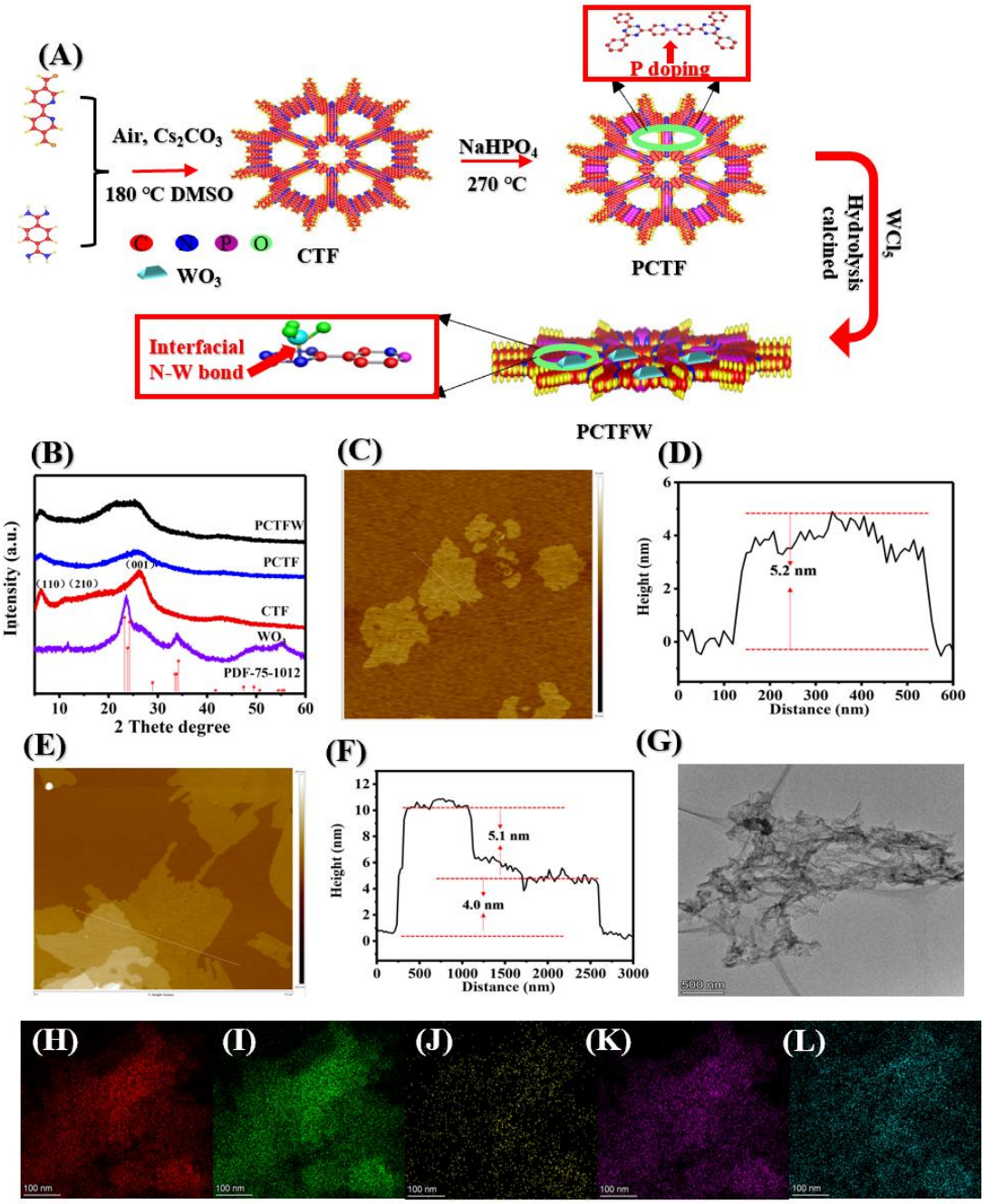

Figure 1. (A) Schematic illustration for the formation of PCTFW. (B) XRD spectrum of as-prepared samples. AFM images of (C, D) CTF and (E, F) PCTFW; TEM images of (G) PCTFW. Elemental mapping of PCTFW (H) C, (I) N; (J) P; (K) O and (L) W.

The synthesis route of PCTFW is displayed in **Figure 1A**. Firstly, CTFs were synthesized by an alcohol oxidation strategy in the open atmosphere. Next, PCTFs were prepared by a directly in-situ high-temperature phosphating method. Then PCTFW was prepared by in-situ hydrolysis of WCl_5 and high-temperature calcination on the surface of

PCTFs. X-ray diffraction (XRD) tested the structural simulations of the as-prepared photocatalysts were tested by X-ray diffraction (XRD). As displayed in **Figure 1B**, the peaks located at 7.1°, 13.1°, and 26.8° are attributed to the (110), (210), and (001) planes of CTF[11], respectively. The PCTF has XRD peaks similar to those of CTF, indicating that the incorporated P atoms hardly influence the crystal structure of CTF. No distinct peak of WO_3 is found in the XRD patterns of PCTFW due to the low contents of WO_3. Through ICP tests, the weight content of WO_3 was 3.12 wt%. The thickness of CTF was determined to be 5.2 nm. After high-temperature phosphating, the thickness of CTF remains 5.1 nm. After in-situ hydrolysis of WO_3 on the surface of PCTF, the thickness of PCTFW was about 9.3 nm. Thus, the thickness of WO_3 was about 4.1 nm. (**Figures 1C-F, and S1**) A scanning electron microscope (SEM) studied the morphology of the as-prepared samples. All samples exhibit nanostructures without specific morphological features (**Figures S2-4**). All the prepared samples show typical two-dimensional nanosheet morphology in the TEM images (**Figures 1G** and **S5-7**). In addition, after P incorporation into the CTF, no noticeable change could be found compared with pure CTF, which indicates that the high-temperature phosphating process did not influence the CTF. For the PCTFW, it could be found that well-defined WO_3 nanosheets with an average diameter of 50-60 nm were uniformly dispersed on CTF surfaces. No lattice fringe could be found on the surface of PCTFW, which indicates that both CTF and WO_3 were amorphous. The EDX elemental mapping results confirm the uniform dispersion of W, O, C, P and N elements in the PCTFW (**Figures 1H-J**). The surface area and pore sizes were tested by N_2 sorption at 77K. The BET surface area and pore volume at P/P_0 of CTF were 64.5096 m^2/g and 0.3302 cm^3/g, respectively. After P incorporation into the layer of PFCOFs, the BET surface area and pore volume display little change, which was 61.9064 m^2/g and 0.3198 cm^3/g, respectively. After combing with WO_3, BET surface area and pore volume decreased to 42.0391 m^2/g and 0.2266 cm^3/g, respectively. Meanwhile, pore sizes of CTF, PCTF and PCTF are all between 3 to 10 nm. All CTF, PCTF and PCTFW were

displayed Type -II adsorption isotherms, suggesting a porous feature[12]. (**Figure S8** and **Table S1**) As displayed in **Figure S9**, CTF displays a major content loss starting at 450 °C. PCTF exhibits superior structural stability with a significant content loss starting at 550 °C. Therefore, P incorporation could enhance the thermal stability of CTF.

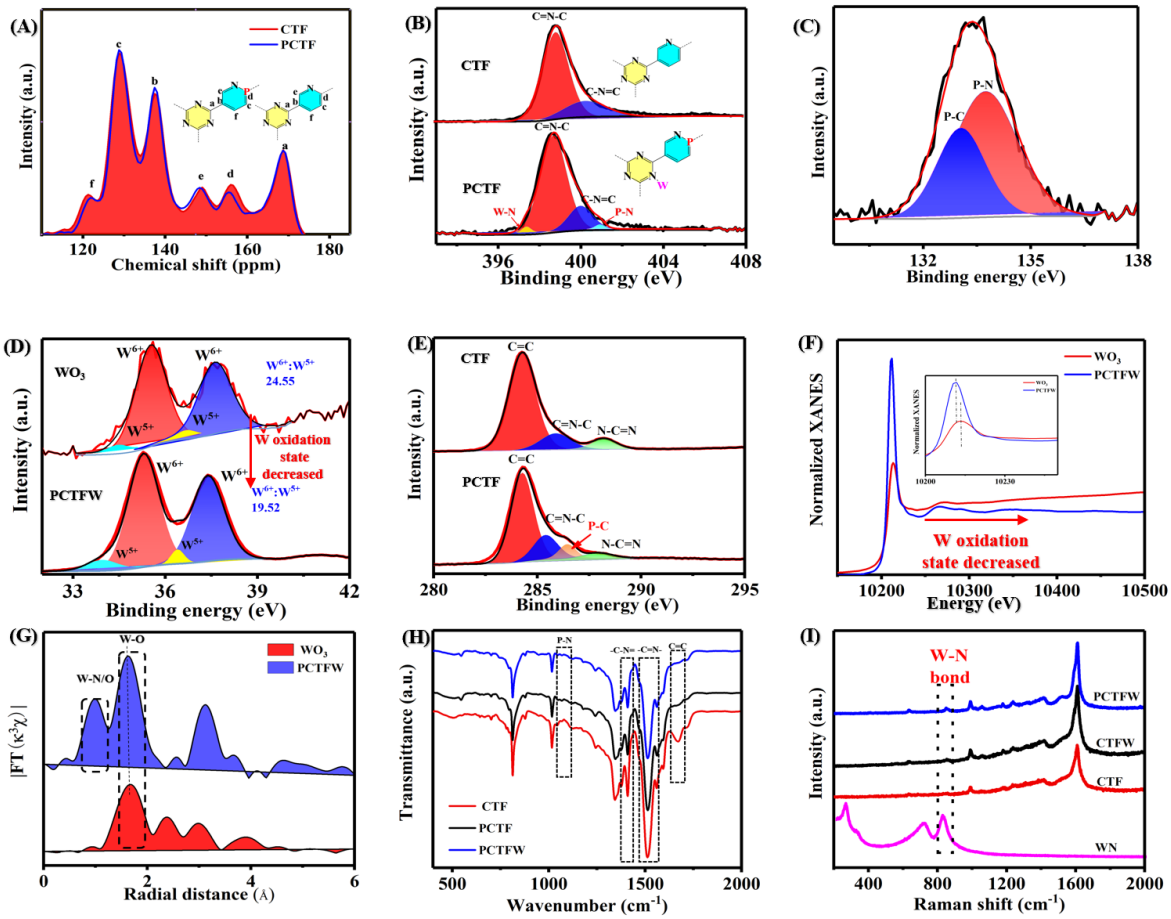

Figure 2. (A) Solid-state 13C CP-MAS NMR of CTF and PCTF; (B)N 1s XPS spectrum of CTF and PCTFW; (C) P 2p XPS spectrum of PCTFW; (D) W 4f XPS spectrum of PCTFW and WO_3; (E) C 1s XPS spectrum of CTF and PCTFW; (F) XANES and (G) k^3 -weighted FT-EXAFS curves of the CTF and WO_3 at W L_3-edge; (H) Raman spectra of the WN, CTF, PCTF and PCTFW; (I) FTIR images of CTF, PCTF and PCTFW.

Solid-state 13C CP/MAS spectra confirmed the successful synthesis of the photocatalysts and P-doped site. As displayed in **Figure 2A**, the chemical shifts at about

168.9 ppm could be attributed to the triazine-ring carbons. Two chemical shifts corresponding to the carbons in benzene rings are located at about 137.2 and 128.5 ppm. The chemical shift at 165 ppm for PCTF shows poor intensity compared with pure CTF, indicating that P has been incorporated at the E sites of C=N-C.[13] In 31P NMR spectrum, two peaks at about −13.2 and 5.3 ppm were assigned to the P-N and P=O in the PCTFW (**Figure S10**). Furthermore, in the N1s XPS spectrum, the peak located at about 398.7 eV for CTF and PCTFW corresponds to pyridine nitrogen (C=N-C) in CTF[11] (**Figure 2B**). Two peaks at about 397.3 and 400.1 eV correspond to the N-W and N-P bonds [14]. The peaks around 133.1 and 133.8 eV for PCTFW are attributed to P-C and P-N bonds, [15] respectively (**Figure 2C**). The formation of the W-N bond and P-C bonds could also be detected in the W 4f and C 1s spectra for PCTFW. In the W 4f spectrum, the 34.85 and 37.07 eV peaks belong to the W $4f_{7/2}$ and W $4f_{5/2,}$ respectively. Two peaks at 33.4 and 35.9 eV are attributed to the W^{5+}. The formation of N-W bonds decreased the W oxidation state. We fit the W 4f XPS spectrum and calculated W^{6+}/W^{5+} ratios by the area ratios of corresponding peaks. It could be found that the formation of N-W bonds decreased the W oxidation state compared with pure WO_3. In the C1s spectrum, the peaks located about 284.2, 285.3, 286.4 and 287.9 eV correspond to C=C, C=O, P-C and N=C-N, respectively.[14, 16] (**Figure 2D-E**). X-ray absorption fine structure (XAFS) further analyse the electric structure of W in PCTFW. The W L_3-edge XANES spectrum of WO_3 and PCTFW are exhibited in **Figure 2F**. The peak located at about 10200 eV was attributed to the electron transitions from the $2p_{3/2}$ state to a vacant 5d state.[17] PCTFW displayed lower white line intensity than WO_3, which suggests a cationic environment. This result suggested the decreased oxidation state of W after forming N-W bonds.[18] In the Fourier transform (R-space, **Figure 2G)** of the (extended X-ray absorption fine structure) EXAFS data for the PCTFW and WO_3. A prominent peak located at about 1.68 Å could be attributed to the W-O bond.[19] In particular, the peak at about 1.25 Å in PCTFW corresponds to the W-O/N coordination, [19a] giving powerful evidence for the formation of

N-W bond between PCTF and WO_3. Then we further recorded the FTIR to confirm the formation of PCTFW (**Figure 2H**). The peaks located at 1508 and 1407 cm^{-1} could be attributed to -C-N= and -C=N-, which suggest the successful synthesis of CTF.[20] Notably, the intensity of C=C, -C-N= and -C=N- had decreased after the phosphorating treatment, which suggests that the P atoms substitute the C atoms near dipyridyl. The additional weak peak at 1070 cm^{-1} is attributed to the P−N stretching mode[21]. In the Raman spectrum (**Figure 1I**), W-N-W stretching vibrations raised from the optic branches near 800 cm^{-1}[22]. This rusult suggests that the successful formation of W-N between PCTF and WO_3.

2. 2 Evaluation of Photocatalytic evolution performance

Ultraviolet-visible diffuse reflectance spectra tested the optical properties of the samples (**Figure 3A**). Pure CTF and WO_3 displayed the absorption edge at around 760 and 550 nm. PCTF and PCTFW could absorb a wider light spectrum up to around 780 nm. Thus, the bandgap of CTF, WO_3, and PCTF were 2.20, 2.41, and 2.06 eV, respectively (**Figure 3B**). Through the VB-XPS test, the VB level of CTF, PCTF, and WO_3 are 1.28, 1.48, and 2.45 eV, respectively (**Figure S11-13**). Therefore, The CB level of CTF, WO_3 and PCTF are -0.92, -0.58 and 0.04 eV, respectively. After P incorporation in the CTF, both CB and VB levels became more negative (**Figure 3C**).

The photocatalytic performance of as-prepared CTF-based photocatalysts was tested in the presence of a TEOA solution. As displayed in Figure 3D, the hydrogen evolution rate of CTF could reach 8.6 μmol h^{-1} with 3% Pt serving as cocatalysts. P incorporation in CTF can result in a dramatic (4.6 times) improvement in photocatalytic performance. This result indicates that the introduction of P could simultaneously boost photocatalytic performance over CTF, the photocatalytic performance of PCTFW-Pt could reach up to 134.84 μmol h^{-1}

(67.42 mmol $h^{-1}g^{-1}$) due to the formation of chemically bonded Z-scheme heterojunction, which is 3.4 and 6.48 times higher than those of PCTF-Pt and CTFW-Pt, respectively. Meanwhile, the photocatalytic hydrogen evolution rate for PCTFW with N-W bond is much better than that of PCTFW without N-W bond. (**Figure S14**) Many external factors, such as surface area, light power density, photocatalysts' mass and temperature, may affect photocatalytic performance[23]. Therefore, using the units (i.e., μmol g^{-1} h^{-1}) to express the photocatalytic performance of the samples is not accurate. Here, we combined the photocatalytic activity with both mass of photocatalysts and per unit surface area of the CTF, PCTF and PCTFW, considering a more favorable method for expressing the actual photocatalytic activity over as-prepared samples (**Figure S15**). The hydrogen evolution per surface area of PCTFW was 1.6 mmol $h^{-1}m^2$, 4.1 and 24.1 times higher than that of pure CTF and PCTF, respectively, consistent with the hydrogen evolution rate per unit mass. We tested the photocatalytic performance of as-prepared samples over the different masses of photocatalysts to determine the light-shielding effect during the photocatalytic process. The photocatalytic hydrogen-evolution rate was not linearly related to the mass of the photocatalyst (**Figure S16**). **Figure S17** displayed the photocatalytic hydrogen evolution based on the weight ratio between the PCTF and WO_3. It indicated that the weight ratio between PCTF and WO_3 with 20:3 displayed the highest HER. Moreover, pure CTF displayed poorer photocatalytic stability than PCTFW (**Figure 3E** and **Figure S18**), indicating that P incorporation and Z-scheme heterojunctions could improve photocatalytic activity and stability over CTF photocatalysts. XPS and XRD results for PCTFW after the photocatalytic reaction demonstrate good stability for PCTFW during the photocatalytic reaction (**Figure S19-20**). The apparent quantum efficiency (AQE) of PCTFW-Pt was 37.63% at 420 nm. Usually, the AQE depended on the usage of photocatalysts. We have tested the AQE based on different usage of catalysts (**Figure 3F**). The photocatalytic performance of PCTFW is higher than most of the hydrogen-evolution CTF-based photocatalysts reported, compared with

constructing molecular heterostructures[24] (6.6 mmol g^{-1} h^{-1}), donor-acceptor structures[25] (19.6 mmol g^{-1} h^{-1}), microwave-assisted synthetic strategy[26] (7.97 mmol g^{-1} h^{-1}) and crystalline covalent triazine frameworks[27] (9.2 mmol g^{-1} h^{-1}) method for constructing high-efficient CTF-based photocatalysts (Please see **Figure 3G** and **Table S2** for a complete comparison).

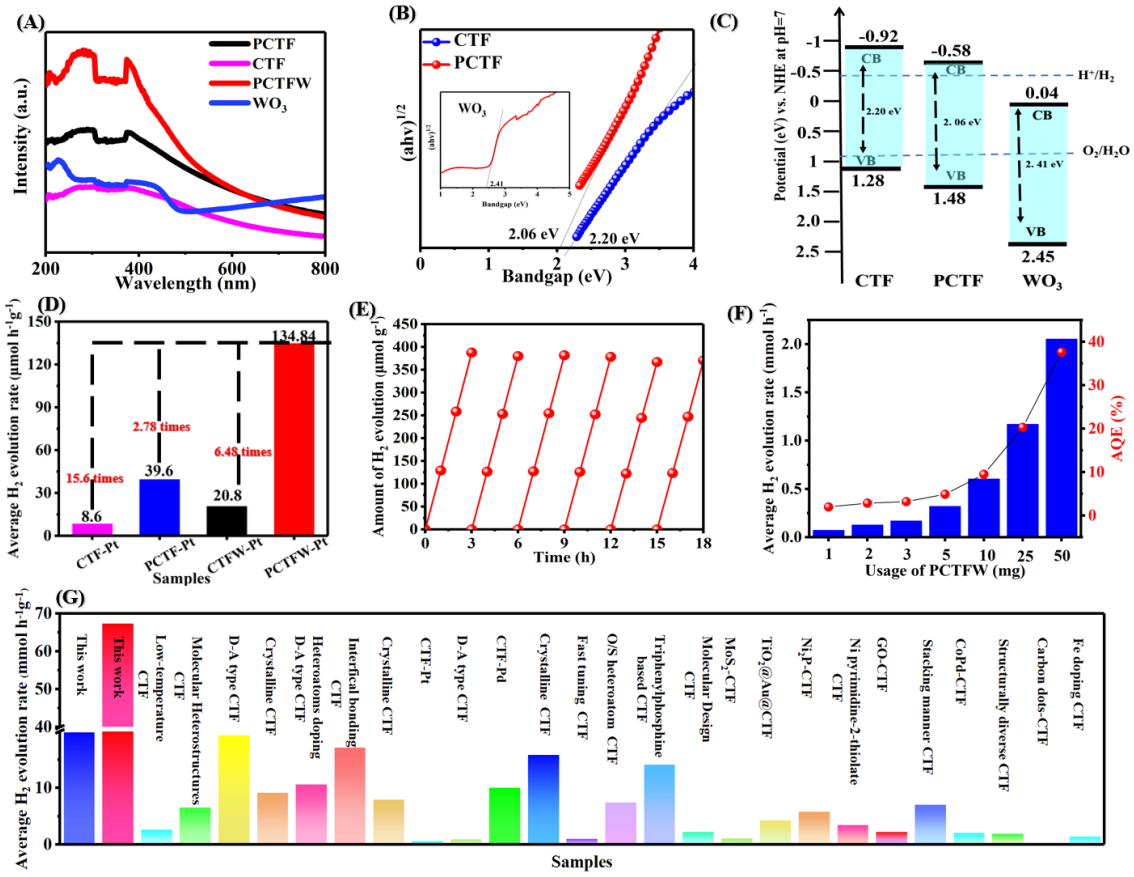

Figure 3. (A) UV-vis DRS patterns of CTF, PCTF, PCTFW and WO_3; (B) Bandgap of CTF and PCTF (insert: WO_3). (C) Band level of CTF, PCTF and WO_3; (D) Average hydrogen-generation rate of CTF, PCTFW, CTFW and PCTFW under visible light ($\lambda \geq 420$ nm); (E) Cyclic H_2 evolution over PCTFW; (F) Average hydrogen evolution and AQY over different amounts of PCTFW; (G) Summary of the photocatalytic H_2 evolution on CTF-based photocatalysts.

2. 3 Mechanism insights on photocatalytic hydrogen evolution enhancement

Exciton dissociation and charge separation are essential for comprehending the photocatalysis process. We measured temperature-dependent PL measurements to test the exciton binding energies. (**Figure 4 A-D** and **S21**) The intensity of PL for CTF, PCTF and PCTFW decreased with the temperature, corresponding to w thermally activated nonradiative recombination process[9b]. The exciton binding energies could be calculated as follows.

$$I(T) = \frac{I_0}{1 + Ae^{-E_b/k_B T}}$$

Where, the I_0, A *and* E_b are the intensity at 0 K, Boltzmann constant and exciton binding energies, respectively. Therefore, the exciton binding energies of CTF and PCTF 322 and 208 meV, respectively, indicate that the excitons in PCTF are more liable to dissociation and thus enhance the contents of free charge carriers for PCTF and result in its high photocatalytic performance.

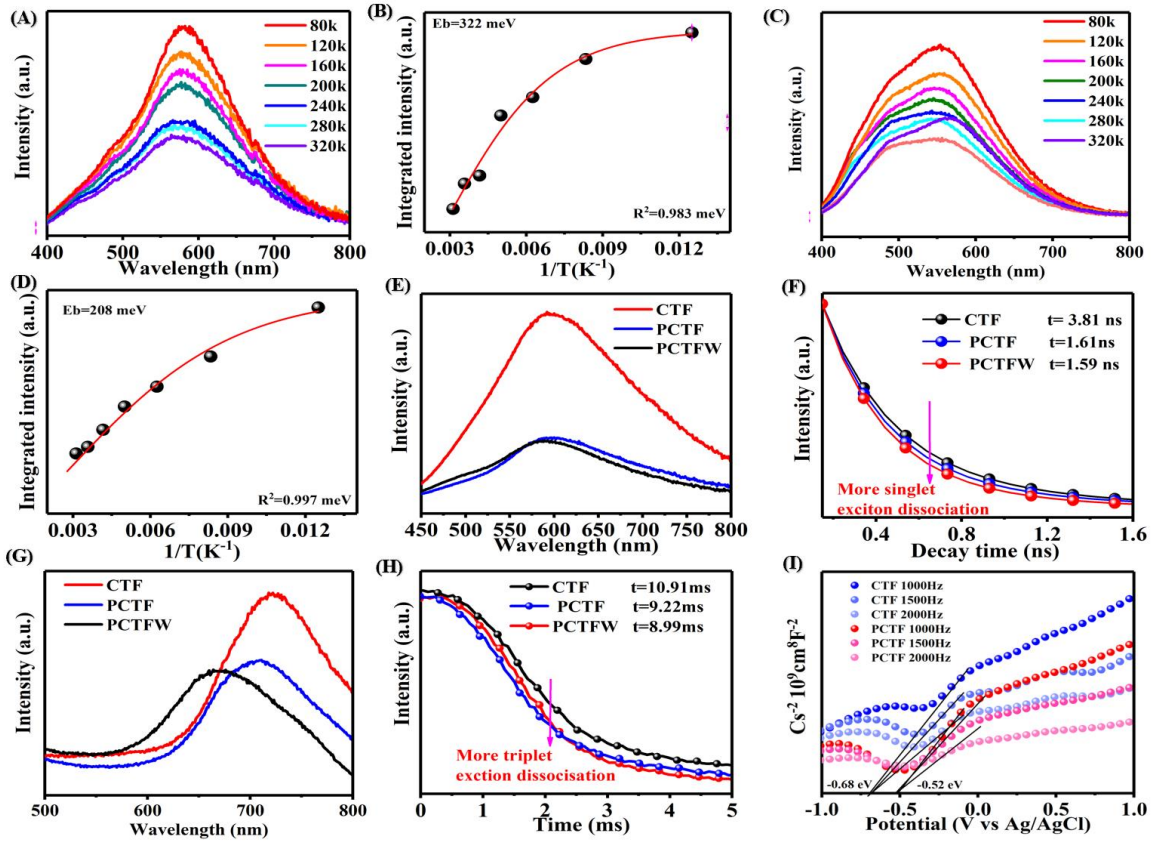

Figure 4. Temperature-dependent PL spectra with excitation wavelength at 380 nm and extracted exciton binding energies of (A), (B) CTF and (C), (D)PCTF. (E) Steady-state fluorescence spectra with a 1 ms delay and (F) time-resolved fluorescence kinetics for CTF, PCTF and PCTFW. (G) low-temperature steady-state phosphorescence recorded at a delayed time of 10 μs and (H) time-resolved phosphorescence kinetics for CTF, PCTF and PCTFW. (I) Mott–Schottky curves of CTF and PCTF.

The P incorporation significantly affects the exciton dissociation processes in CTF. We used photoluminescence measurements to understand the exciton dissociation processes. [5] As shown in **Figure 4E**, the steady-state prompt fluorescence spectra measured at 300 K show that PCTF significantly reduced emission compared with CTF. The fluorescence signals are produced from the radiative decay of singlet excitons in the CTF. The decreased intensity means the efficient reduction and dissociation of singlet excitons. The lifetime of CTF and PCTF fit by steady-state emission was 3.81 and 1.61 ns, respectively. (**Figure 4F**) The significantly reduced lifetime of singlet exciton indicates improved singlet exciton dissociation in the PCTF[5]. We future analyze the triplet excitons by delayed phosphorescence[28]. With a 1 ms delayed time, the CTF sample exhibits an emission peak at about 721 nm. After P incorporation, the PCTF displayed a blue shift at around 710 nm with lower phosphorescence intensity. (**Figure 4G**) The considerable difference between CTF and PCTF indicated the strong correlation between heteroatoms-induced emission and exciton dissociation. PCTF displayed faster phosphorescence decay confirming the promoted exciton dissociation induced by P incorporation[7]. (**Figure 4H**) In addition, the low singlet and triplet excitons would reduce excitonic interactions and result in high excited-species quantum yields. The electron concentration could be calculated by its slope in Mott–Schottky curves. Based on Mott–Schottky equation (**Figure 4I**), the electron concentration of PCTF is higher than that of CTF[5]. The above results confirm the P-incorporation-induced exciton

dissociation in CTF. The formation of Z-scheme heterojunction shows little influence in excitons dissociation.

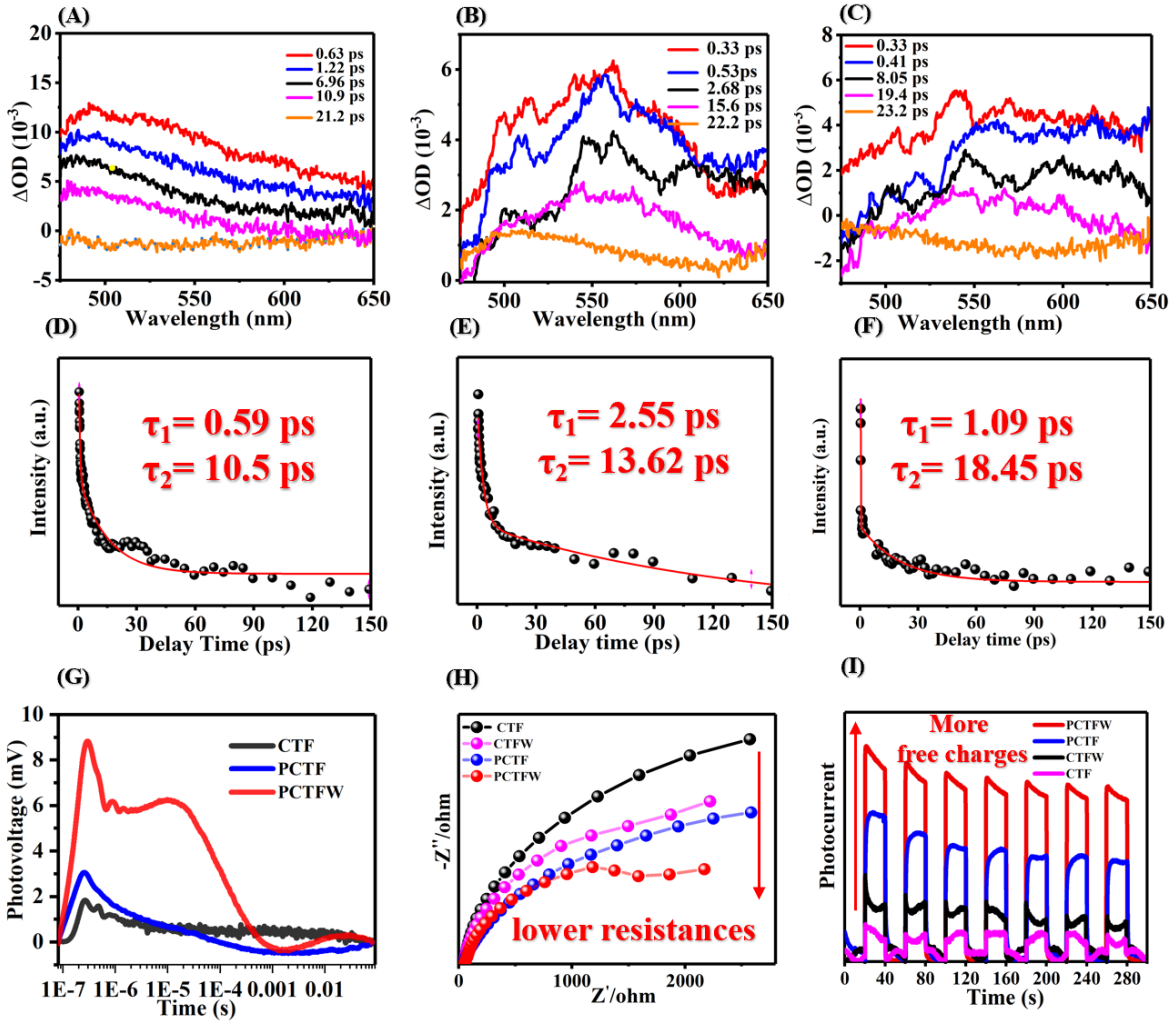

Figure 5. Transient absorption spectra of (A) CTF, (B) PCTF and (C) PCTFW; Time profiles and fitted decay kinetics of transient absorption of (D) CTF, (E PCTF and (F) PCTFW; (G) Transient photovoltage response with a laser wavelength of 355 nm; (H) Photocurrent and (I) Emission spectra of as-prepared CTF, PCTF and PCTFW photocatalysts.

We tested femtosecond transient absorption spectroscopy to analyze the separation of photogenerated electron-hole pairs and the charge migration dynamic of CTF, PCTF and PCTFW at ps timescale. As shown in **Figure 5 A-F**, both PFCOF and PCTFW show a negative band at 480-550 nm, corresponding to excited-state absorption (ESA) [29], which corresponds to photogenerated charges of charge pairs in the CTF part of the system[30].

Compared to pure CTF, both PCTF and PCTFW display much stronger and longer-lived absorption for their ESA. To better understand the dynamic of electrons separation and migration, the kinetics at 500 nm (for CTF) and 550 nm (for PCTF and PCTFW) were measured in Figure 5D-F. The decay trace at 500 nm was analyzed using a bi-exponential. The τ_1 and τ_2 of pure CTF were 0.59 and 10.9 ps, corresponding to the recombination of the free photogenerated electron-hole pairs and the shallow charge trapping, respectively.[31] Usually, the recombination of the photogenerated electron-hole pairs is too fast to weaken the migration of the photogenerated electrons. Therefore, the migration of photogenerated electrons should be trapped by the shallow state immediately, where they would have high mobility and driving force for photocatalytic hydrogen evolution[32]. For the PCTF, the enhanced lifetimes of τ_1 (2.55 ps) could be attributed to the improved possibility of the active electrons utilization and migration to other electron acceptors due to the P incorporation in CTF, effectively enhancing the in-built electric field to accelerate electrons transfer. The increased τ_2 (13.62 ps) helps transfer the active electrons and boost photocatalytic hydrogen-evolution performance. Therefore, PCTF displayed higher photocatalytic performance than CTF. For the PCTFW, the τ_1 (1.09 ps) corresponds to the recombination of electron-hole pairs at the interface between the PCTF and WO_3, the τ_2 (18.45 ps) could be attributed to the transfer of electrons from the CB of WO_3 to the VB of PCTF and then combine with the hole in the PCTF.[33] To deeply understand the excellent performance of PCTFW and probe its internal electron transfer dynamics, transient surface photovoltage spectroscopy was carried out. The intensity of the photovoltage signal correlates with the separation efficiency of photogenerated electron-hole pairs[34]. The intensity of PCTF and PCTFW is significantly stronger than that of CTF, suggesting that the separation efficiency of CTF has dramatically improved after P incorporation and forming a Z-scheme heterojunction (**Figure 5G**).

Transient surface photovoltage spectroscopy further revealed the kinetics feature of photogenerated charges. It could be found that the scope of the time value is less than 10^{-6} s,

and the surface photovoltage responses of the PCTF and PCTFW are higher than CTF. The photogenerated electron-hole pairs in PCTF and PCTFW can be separated effectively because of built-in electric fields. The intensity of transient surface photovoltage gradually decreases, attributed to the recombination process of photogenerated electron-hole pairs. The longer delay time of the retardation peaks means a slower recombination rate of the photogenerated electrons and holes. Thus, P incorporation and Z-scheme heterojunction could effectively accelerate electron-hole separation and prolong the lifetime of photogenerated electrons. The high photocurrent for both PCTFW and PCTF indicates that more excitons can be effectively dissociated into carriers by P incorporation (**Figure 5H**). Similarly, the smaller radius of PCTFW in the EIS Nyquist plots indicates the lower resistance for the interfacial charge separation[35] (**Figure 5I**).

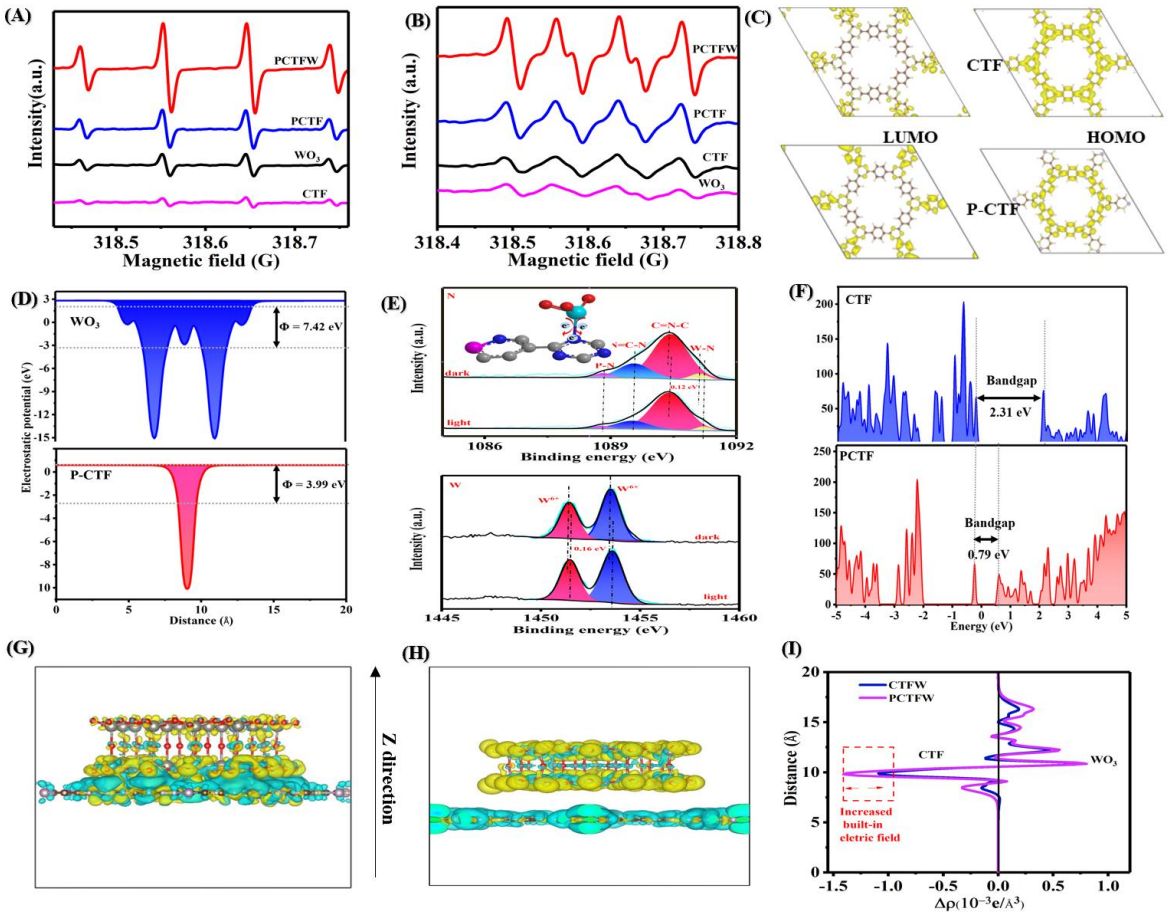

Figure 6. EPR signals of (A)DMPO-$O_2^{\bullet-}$ and (B) DMPO-$OH^{\bullet}$ adducts in methanol. (C) Isosurface of molecular orbital distribution of proposed fragments of CTF and PCTF; (D)

Total density of states and partial density of states of CTF and PCTF; (E) High-resolution XPS for N 1s W 4f of PCTFW in the dark as well as under 420 nm visible-light irradiation; (F) Electrostatic potentials of WO_3 and PCTF; Planar-averaged electron density difference Dr(z) for PCTFW with N-W bond (G) and PCTFW without N-W bond (H); (I) The charge density difference for PCTFW and CTFW.

The formation of Z-scheme heterojunctions effectively accelerates the separation of photogenerated electron-hole pairs. We further confirmed the formation of Z-scheme heterojunctions by experiment and DFT calculation. The CB and VB levels of PCTF match well with those of WO_3, facilitating the formation of Z-scheme heterojunction. We first measured UPS and electron paramagnetic resonance (EPR) results to confirm the formation of Z-scheme heterojunctions. As displayed in **Figure 6A-B**, PCTFW displayed the strongest signals of $OH^{\bullet}$ and $O_2^{\bullet-}$. Meanwhile, the signals of $OH^{\bullet}$ and $O_2^{\bullet-}$ of PCTF were stronger than those of CTF, which indicates that the PCTF has a much stronger oxidation-reduction ability than CTF[36]. UPS was used to detect the Femi level of the as-prepared photocatalysts (**Figure S22**). The work functions of CTF, PCTF and WO_3 were 3.72, 3.91 and 4.28 eV, respectively. Therefore, the Femi level of CTF, PCTF and WO_3 were -3.71, -3.92 and -4.28 eV, respectively.[37] We measured the in-situ XPS to determine the electron transfer pathway between PCTF and WO_3 (**Figure 6D**). W 4f spectrum displays an obvious positive shift (0.16 eV) under visible light irradiation, suggesting a decreased W electron density.[38] In the N1s spectrum, an 0.12 eV negative shift could be observed under light irradiation (W-N bond and C-N=C site), which suggests that electrons transfer from the WO_3 to the N sites in the triazine via the W-N bonds (**Figure 6D insert**). The work functions of CTF and WO_3 were determined to be 3.99 eV and 7.42 Ev by DFT calculation, respectively, which was consistent with the experiment results (**Figure 6E**). According to the DFT results, the triazine units belong to HOMO orbitals, meaning that the W-N bond connects the CB of WO_3 and VB of PCTF. Therefore, the electrons transferred from the WO_3 will be directly injected into the VB

of CTF via the W-N bond and directly recombined with the holes in the CTF. (**Figure 6C and S23**) The electrons will be transferred from the PCTF to the WO_3 until the Femi levels are equilibrated with an internal electric field from the positively charged surface of CTF to the negatively charged surface of WO_3. Under visible light irradiation, the photogenerated electrons at the CB of WO_3 will be recombined with the holes in the HOMO of CTF due to the internal electric field.

To better understand the role of P incorporation and Z-scheme heterojunctions in PCTFW, DFT calculations were conducted. As displayed in **Figure 6F**, an impurity level has been created after P incorporation into the CTF, which decreases the bandgap of CTF and serves as the photogenerated carrier trap sites to prolong the lifetime of photogenerated electrons. Thus, the visible-light absorption of PCTF was better than that of CTF and the lifetime of photogenerated electrons of PCTF was longer than that of CTF, which is consistent with the experimental results. In addition, as shown in **Figure 6C**, the HOMO and LUMO are distributed together in the CTF. However, the dipyridyl could serve as the electron acceptor after P incorporation in the CTF. The triazine can function as an electron donor, with the benzene acting as the bridge to transfer electrons from donors to acceptors in the push-pull interaction. Therefore, the HOMO and LUMO levels are effectively separated. This structure displays a more efficient charge separation ability via HOMO−LUMO transition. The effective separation of HOMO and LUMO suggests that the P incorporation may have a more efficient charge separation ability via HOMO−LUMO transition, consistent with the photocatalytic performance. The 3D charge density difference was measured to determine the separation and migration of the electron at the interface of PCTFW. The charge accumulation is shown in **figure 6G** as the yellow region, and the charge depletion is shown as the cyan region. Charge redistribution mainly occurred around the WO_3/PCTF interface. In contrast, few charges accumulate at the interface, indicating that forming N-W bond could accelerate charge transfer at the interface (**Figure 6H**). Meanwhile, the charge density change was

observed in the inner WO_3 due to forming the W-N bond between PCTF and WO_3. **Figure 6I** displays the planar-averaged charge density along the Z direction. The carriers transfer from PCTF to WO_3 via W-N bond due to the charge density difference at the interface of PCTF and WO_3 and the holes stay in the CTF simultaneously. When charge density receives equilibrium states, a built-in electric field is constructed due to the net charge accumulation at the interface of PCTF and WO_3 with the direction from the PCTF to the WO_3, which is beneficial for separating photogenerated electron-hole pairs. In addition, the intensity of the built-in electric field for PCTFW is stronger than that of CTFW due to the P incorporation. This means that the transfer of photogenerated carriers in PCTFW has a stronger thermodynamic driving force.

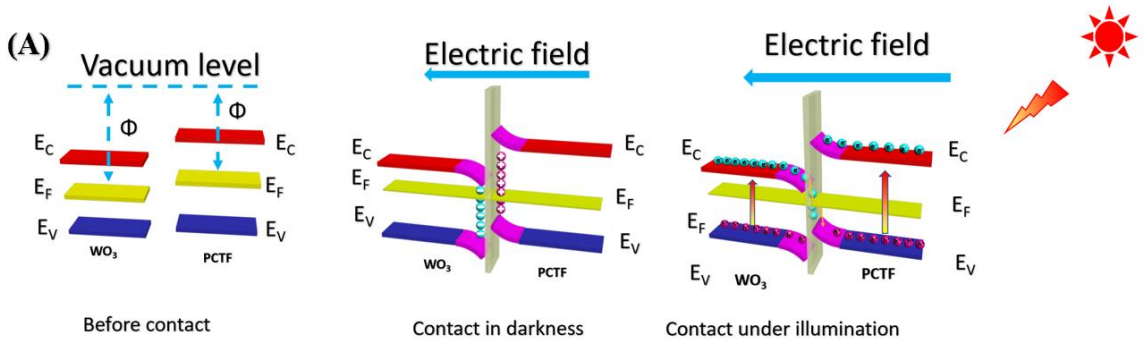

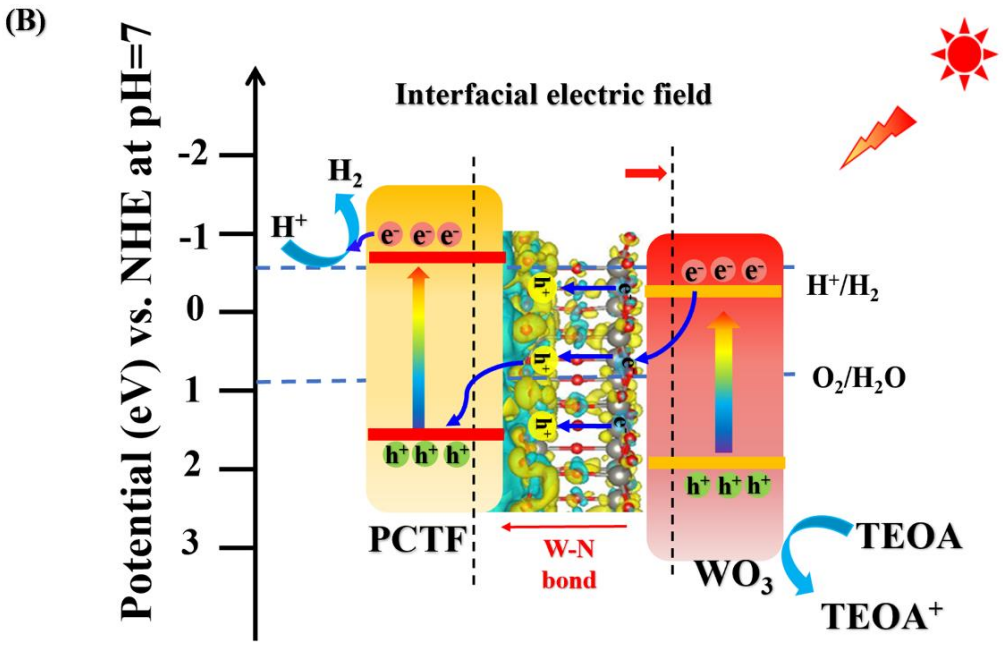

Figure 7. (A) Schematic illustration of Z-scheme charge transfer process; (B) Schematic illustration for the photocatalytic mechanism of PCTFW.

Concluding the above theoretical calculations and experimental results, we can depict the mechanism of enhanced photocatalytic performance of PCTFW in **Figure 7**. Upon the intimate contact between PCTF and WO_3, the electrons in the PCTF will transfer to the WO_3 until the equilibrated Femi level is reached.[39] An internal electric field is constructed between the PCTF and WO_3. Under visible light irradiation, both PCTF and WO_3 generated electrons from the VB to the CB while the holes remained in the VB (**Figure 7A**). Induced by the internal electric field, the photogenerated electrons in the CB of WO_3 would recombine with the holes in the VB of PCTF to follow the W-N chemical bond. This maximizes the utilization of the electrons in the CB of PCTF in the reduction reaction and the holes in the VB of WO_3 for the oxidation reaction. These results confirmed the successful construction of Z-scheme heterojunction between PCTF and WO_3. Due to the successful doping of P, the internal electric field is enhanced, which enhances the exciton dissociation and charge transfer driving force. Therefore, more free charges are generated from exciton dissociation and transfer to the CB of PCTF and VB of WO_3 to take place redox reaction. (**Figure 7B**)

3. Conclusions

In summary, Phosphorus-incorporated Z-scheme heterojunctions (PCTFW) have been successfully synthesized by in-situ hydrolysis and a high-temperature phosphating method. It is worth noting that the introduced P atoms could simultaneously optimize energy band structures, enhance built-in electric fields and induce excitons to dissociate into charge carriers of CTF effectively. High-quality interfacial W-N bonds improve the interfacial transfer of photogenerated electrons, thus prolonging the lifetime of photogenerated electrons. Consequently, the photocatalytic H_2 evolution rate of PCTFW could reach up to 67.42 $mmolh^{-1}g^{-1}$ with an apparent quantum efficiency of 37.63% at 420 nm. This work demonstrates the importance of exciton dissociation and charges separation at atomic level

interfaces in improving the photocatalytic H_2 evolution, which will shed light on developing promising CTF-based photocatalysts.

4. Experimental Section

Synthesis of CTF: mmol of [2,2'-bipyridine]-5,5'- diyldimethanol, 2.0 mmol terephthalamidine dihydrochloride and 4.4 mmol of cesium carbonate were added into the DMSO in a round-bottom flask. The mixture was heated through a temperature-programmed route by stirring at 100°C for 12 h, 120°C for 12 h, 140°C for 12 h and 180°C for 48 h. Then the mixture was washed with water, ethanol, and tetrahydrofuran. The final yellow samples were freeze-dried for 24 h to obtain CTF (82% yield)

Synthesis of P-CTF: The as-prepared CTF (20 mg) and NaH_2PO_2 (200 mg) were mixed and calcined at 270℃ for 2h under an Ar atmosphere. The resulting samples were washed with DI water and ethanol three times.

Synthesis of CTF-WO_3: 100 mg of as-prepared CTF was firstly dispersed in ethanol. Then 15 mg of WCl_5 was added into the suspension and sonicated for another 10 min. Next,10 ml distilled water add to the suspension and keep the string for 1 hour. After centrifuging and washing with ethanol and water, the CTF-WO_3 aquo-complex products were freeze-dried. Finally, the CTFW was obtained by heating the CTFW aquo-complex at 270 ℃ for 2h at Ar atmosphere.

Synthesis of P-CTF-WO_3: 100 mg of as-prepared P-CTF was firstly dispersed in ethanol. Then 15 mg of WCl_5 was added into the suspension and sonicated for another 10 min. Next,10 ml distilled water add to the suspension and keep the string for 1 hour. After centrifuging and washing with ethanol and water, the CTF-WO_3 aquo-complex products were freeze-dried. Finally, the CTFW was obtained by heating the CTFW aquo-complex at 270 ℃ for 2h at Ar atmosphere.

Author Contributions

Rongchen Shen and Xin Li designed the systems, synthesized the photocatalysts, performed the experimental measurement, analyzed the data as well as wrote the manuscript. Xiuzhi Li, Chaochao Qin carried out transient absorption spectroscopy experiments. Peng

Zhang analyzed experimental data. Neng Li carried out the computational studies. Junwang Tang helped to analyze the data and revise the manuscript.

Acknowledgements

X.Li thanks National Natural Science Foundation of China (21975084, 51672089) and Natural Science Foundation of Guangdong Province (2021A1515010075) for their support.

[1] a) Z. Yang, H. Chen, S. Wang, W. Guo, T. Wang, X. Suo, D.-e. Jiang, X. Zhu, I. Popovs, S. Dai, *J. Am. Chem. Soc.* **2020**, 142, 6856; b) C. Dai, B. Liu, *Energy Environ. Sci.* **2020**, 13, 24; c) J. Xie, S. A. Shevlin, Q. Ruan, S. J. A. Moniz, Y. Liu, X. Liu, Y. Li, C. C. Lau, Z. X. Guo, J. Tang, *Energy Environ. Sci.* **2018**, 11, 1617; d) L. Zizhan, S. Rongchen, N. Yun Hau, F. Yang, M. Tianyi, Z. Peng, L. Youji, L. Xin, *Chem. Catal*, **2022**, 2, 2157; e) Z.-A. Lan, M. Wu, Z. Fang, Y. Zhang, X. Chen, G. Zhang, X. Wang, *Angew. Chem. Int. Ed.* **2022**, 61; f) Z.-A. Lan, X. Chi, M. Wu, X. Zhang, X. Chen, G. Zhang, X. Wang, *Small* **2022**, 18, 2200129; g) R. Sun, B. Tan, *Chemistry-a European Journal* **2023**, e202203077.

[2] O. V. Mikhnenko, P. W. M. Blom, T. Q. Nguyen, *Energy Environ. Sci.* **2015**, 8, 1867.

[3] M. Rahman, H. Tian, T. Edvinsson, *Angew. Chem. Int. Edit.* **2020**, 59, 16278.

[4] a) J. Kosco, S. Gonzalez-Carrero, C. T. Howells, T. Fei, Y. F. Dong, R. Sougrat, G. T. Harrison, Y. Firdaus, R. Sheelamanthula, B. Purushothaman, F. Moruzzi, W. D. Xu, L. Y. Zhao, A. Basu, S. De Wolf, T. D. Anthopoulos, J. R. Durrant, I. McCulloch, *Nature Energy* **2022**, 7, 340; b) J. Kosco, M. Bidwell, H. Cha, T. Martin, C. T. Howells, M. Sachs, D. H. Anjum, S. Gonzalez Lopez, L. Y. Zou, A. Wadsworth, W. M. Zhang, L. S. Zhang, J. Tellam, R. Sougrat, F. Laquai, D. M. DeLongchamp, J. R. Durrant, I. McCulloch, *Nat. Mater.* **2020**, 19, 559.

[5] H. Wang, X. S. Sun, D. D. Li, X. D. Zhang, S. C. Chen, W. Shao, Y. P. Tian, Y. Xie, *J. Am. Chem. Soc.* **2017**, 139, 2468.

[6] J. Gorenflot, A. Paulke, F. Piersimoni, J. Wolf, Z. P. Kan, F. Cruciani, A. El Labban, D. Neher, P. M. Beaujuge, F. Laquai, *Adv. Energy Mater.* **2018**, 8, 1701678.

[7] Y. Pan, R. Lin, Y. Chen, S. Liu, W. Zhu, X. Cao, W. Chen, K. Wu, W. C. Cheong, Y. Wang, L. Zheng, J. Luo, Y. Lin, Y. Liu, C. Liu, J. Li, Q. Lu, X. Chen, D. Wang, Q. Peng, C. Chen, Y. Li, *J Am Chem Soc* **2018**, 140, 4218.

[8] H. Wang, W. Liu, X. He, P. Zhang, X. Zhang, Y. Xie, *J. Am. Chem. Soc.* **2020**, 142, 14007.

[9] a) J. Xu, C. Yang, S. Bi, W. Wang, Y. He, D. Wu, Q. Liang, X. Wang, F. Zhang, *Angew. Chem. Int. Edit.* **2020**, 59, 23845; b) C. Li, J. Liu, H. Li, K. Wu, J. Wang, Q. Yang, *Nat. Commun.* **2022**, 13, 2357.

[10] a) Y. Yu, W. Yan, X. Wang, P. Li, W. Gao, H. Zou, S. Wu, K. Ding, *Adv. Mater.* **2018**, 30, 1705060; b) S. Guo, Z. Deng, M. Li, B. Jiang, C. Tian, Q. Pan, H. Fu, *Angew. Chem. Int. Edit.* **2016**, 55, 1830; c) D. M. Zhao, Y. Q. Wang, C. L. Dong, Y. C. Huang, J. Chen, F. Xue, S. H. Shen, L. J. Guo, *Nat. Energ.* **2021**, 6, 388.

[11] M. Liu, Q. Huang, S. Wang, Z. Li, B. Li, S. Jin, B. Tan, *Angew. Chem. Int. Edit.* **2018**, 57, 11968.

[12] S. Jhulki, A. M. Evans, X. L. Hao, M. W. Cooper, C. H. Feriante, J. Leisen, H. Li, D. Lam, M. C. Hersam, S. Barlow, J. L. Bredas, W. R. Dichtel, S. R. Marder, *J. Am. Chem. Soc.* **2020**, 142, 783.
[13] L. Hao, J. Ning, B. Luo, B. Wang, Y. B. Zhang, Z. H. Tang, J. H. Yang, A. Thomas, L. J. Zhi, *J. Am. Chem. Soc.* **2015**, 137, 219.
[14] Y. L. Wang, T. Nie, Y. H. Li, X. L. Wang, L. R. Zheng, A. P. Chen, X. Q. Gong, H. G. Yang, *Angew. Chem. Int. Edit.* **2017**, 56, 7430.
[15] a) L. Jing, R. Zhu, D. L. Phillips, J. C. Yu, *Adv. Funct. Mater.* **2017**, 27, 1703484; b) H. Z. Gu, Y. L. Gu, Z. F. Li, Y. C. Ying, Y. Qian, *J. Mater. Res.* **2003**, 18, 2359.
[16] Z. Ai, Y. Shao, B. Chang, L. Zhang, J. Shen, Y. Wu, B. Huang, X. Hao, *Appl. Catal. B-Environ.* **2019**, 259, 118077.
[17] S. Yamazoe, Y. Hitomi, T. Shishido, T. Tanaka, *Journal of Physical Chemistry C* **2008**, 112, 6869.
[18] Z. G. Chen, W. B. Gong, Z. B. Liu, S. Cong, Z. H. Zheng, Z. Wang, W. Zhang, J. Y. Ma, H. S. Yu, G. H. Li, W. B. Lu, W. C. Ren, Z. G. Zhao, *Nano Energy* **2019**, 60, 394.
[19] a) Y. Gu, B. Xi, W. Tian, H. Zhang, Q. Fu, S. Xiong, *Adv. Mater.* **2021**, 33, 2100429; b) W. Chen, J. Pei, C.-T. He, J. Wan, H. Ren, Y. Wang, J. Dong, K. Wu, W.-C. Cheong, J. Mao, X. Zheng, W. Yan, Z. Zhuang, C. Chen, Q. Peng, D. Wang, Y. Li, *Adv. Mater.* **2018**, 30, 1800396; c) R. Shen, L. Zhang, N. Li, Z. Lou, T. Ma, P. Zhang, Y. Li, X. Li, *ACS Catal.* **2022**, 12, 9994.
[20] K. W. Wang, L. M. Yang, X. Wang, L. P. Guo, G. Cheng, C. Zhang, S. B. Jin, B. Tan, A. Cooper, *Angew. Chem. Int. Edit.* **2017**, 56, 14149.
[21] Y. Zhang, T. Mori, J. Ye, M. Antonietti, *J. Am. Chem. Soc.* **2010**, 132, 6294.
[22] a) B. Wicher, R. Chodun, K. Nowakowska-Langier, M. Trzcinski, L. Skowronski, S. Okrasa, R. Minikayev, M. K. Naparty, K. Zdunek, *Vacuum* **2019**, 165, 266; b) A. Aldalbahi, R. Velazquez, A. F. Zhou, M. Rahaman, P. X. Feng, *Nanomaterials* **2020**, 10, 1433.
[23] a) Z. Wang, T. Hisatomi, R. Li, K. Sayama, G. Liu, K. Domen, C. Li, L. Wang, *Joule* **2021**, 5, 344; b) M. Melchionna, P. Fornasiero, *ACS Catal.* **2020**, 10, 5493; c) P. Dong, Y. Wang, A. Zhang, T. Cheng, X. Xi, J. Zhang, *ACS Catal.* **2021**, 11, 13266.
[24] W. Huang, Q. He, Y. Hu, Y. Li, *Angew. Chem. Int. Edit.* **2019**, 58, 8676.
[25] L. Guo, Y. Niu, S. Razzaque, B. Tan, S. Jin, *ACS Catal.* **2019**, 9, 9438.
[26] T. Sun, Y. Liang, Y. Xu, *Angew. Chem. Int. Edit.* **2022**, 61, 202113926.
[27] S. Zhang, G. Cheng, L. Guo, N. Wang, B. Tan, S. Jin, *Angew. Chem. Int. Edit.* **2020**, 59, 6007.
[28] Y. Qan, D. Li, Y. Han, H.-L. Jiang, *J. Am. Chem. Soc.* **2020**, 142, 20763.
[29] Z. Wei, W. Wang, W. Li, X. Bai, J. Zhao, E. C. M. Tse, D. L. Phillips, Y. Zhu, *Angew. Chem. Int. Edit.* **2021**, 60, 8236.
[30] R. Godin, Y. Wang, M. A. Zwijnenburg, J. W. Tang, J. R. Durrant, *J. Am. Chem. Soc.* **2017**, 139, 5216.
[31] A. A. Cordones, C. Das Pemmaraju, J. H. Lee, I. Zegkinoglou, M.-E. Ragoussi, F. J. Himpsel, G. de la Torre, R. W. Schoenlein, *J. Phys. Chem. Lett.* **2021**, 12, 1182.
[32] J. W. Xue, M. Fujitsuka, T. Majima, *ACS Appl. Energ. Mater.* **2019**, 11, 40860.
[33] M. S. Zhu, Z. C. Sun, M. Fujitsuka, T. Majima, *Angew. Chem. Int. Ed.* **2018**, 57, 2160.
[34] a) Z. Y. Liu, D. D. L. Sun, P. Guo, J. O. Leckie, *Nano Letters* **2007**, 7, 1081; b) W. Jiang, J. Low, K. Mao, D. Duan, S. Chen, W. Liu, C. W. Pao, J. Ma, S. Sang, C. Shu, X. Zhan, Z. Qi, H. Zhang, Z. Liu, X. Wu, R. Long, L. Song, Y. Xiong, *J Am Chem Soc* **2021**, 143, 269; c) S. Cao, B. Shen, T. Tong, J. Fu, J. Yu, *Advanced Functional Materials* **2018**, 28, 1800136.
[35] S. Cao, H. Li, T. Tong, H.-C. Chen, A. Yu, J. Yu, H. M. Chen, *Advanced Functional Materials* **2018**, 28, 1802169

[36] J. Wan, L. Liu, Y. Wu, J. Song, J. Liu, R. Song, J. Low, X. Chen, J. Wang, F. Fu, Y. Xiong, *Advanced Functional Materials* **2022**, 32, 2203252.
[37] P. Wang, Y. Mao, L. Li, Z. Shen, X. Luo, K. Wu, P. An, H. Wang, L. Su, Y. Li, S. Zhan, *Angew. Chem. Int. Edit.* **2019**, 58, 11329.
[38] J. Low, B. Dai, T. Tong, C. Jiang, J. Yu, *Adv. Mater.* **2019**, 31, 1802981.
[39] C. Cheng, B. He, J. Fan, B. Cheng, S. Cao, J. Yu, *Adv. Mater.* **2021**, 33, 2100317.